JACS
JOURNAL OF THE AMERICAN CHEMICAL SOCIETY
pubs.acs.org/JACS
Article

Atom-by-Atom Evolution of the Same Ligand-Protected Au_{21}, Au_{22}, $Au_{22}Cd_1$, and Au_{24} Nanocluster Series

Yingwei Li,[$] Michael J. Cowan,[$] Meng Zhou, Tian-Yi Luo, Yongbo Song, He Wang, Nathaniel L. Rosi, Giannis Mpourmpakis,* and Rongchao Jin*

Cite This: https://dx.doi.org/10.1021/jacs.0c09110
Read Online

ABSTRACT: Atom-by-atom manipulation on metal nanoclusters (NCs) has long been desired, as the resulting series of NCs can provide insightful understanding of how a single atom affects the structure and properties as well as the evolution with size. Here, we report crystallizations of $Au_{22}(SAdm)_{16}$ and $Au_{22}Cd_1(SAdm)_{16}$ (SAdm = adamantanethiolate) which link up with $Au_{21}(SAdm)_{15}$ and $Au_{24}(SAdm)_{16}$ NCs and form an atom-by-atom evolving series protected by the same ligand. Structurally, $Au_{22}(SAdm)_{16}$ has an $Au_3(SAdm)_4$ surface motif which is longer than the $Au_2(SAdm)_3$ on $Au_{21}(SAdm)_{15}$, whereas $Au_{22}Cd_1(SAdm)_{16}$ lacks one staple Au atom compared to $Au_{24}(SAdm)_{16}$ and thus the surface structure is reconstructed. A single Cd atom triggers the structural transition from Au_{22} with a 10-atom bioctahedral kernel to $Au_{22}Cd_1$ with a 13-atom cuboctahedral kernel, and correspondingly, the optical properties are dramatically changed. The photoexcited carrier lifetime demonstrates that the optical properties and excited state relaxation are highly sensitive at the single atom level. By contrast, little change in both ionization potential and electron affinity is found in this series of NCs by theoretical calculations, indicating the electronic properties are independent of adding a single atom in this series. The work provides a paradigm that the NCs with continuous metal atom numbers are accessible and crystallizable when meticulously designed, and the optical properties are more affected at the single atom level than the electronic properties.

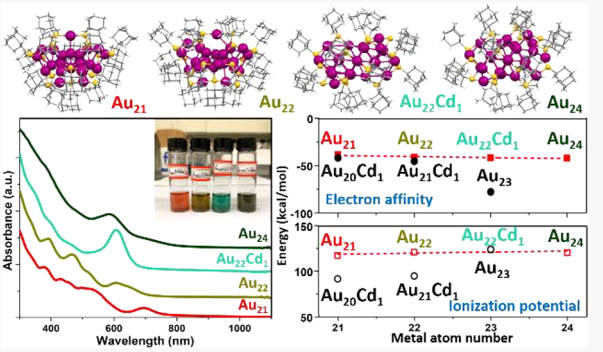

INTRODUCTION

A central task in nanoscience is to create uniform nanostructures and understand their unique properties which are not seen in atoms or bulk counterparts. The investigation on the structure and properties of nanomaterials through atom-by-atom manipulations is highly desirable yet extremely challenging.[1−3] While the atom-by-atom manipulation has been demonstrated in some planar materials,[1−3] it is much harder in nanoparticles (NPs) due to the nonplanar topology, the presence of surfactants or stabilizers, and the illusive surface or interface structure, not to mention the size dispersity of regular NPs.

The recent success in the development of atomically precise nanochemistry has created new opportunities.[4−17] It is now possible to perform atom-by-atom manipulations on atomically precise nanoparticles in the size range from tens to hundreds of metal atoms (equivalently 1−3 nm in diameter). In this size regime, the precision of the number of atoms is important as it decides the structure and the material properties. For example, within a merely 33-atom gap, a sharp transition is observed from nonmetallic $Au_{246}(SR)_{80}$ to metallic/plasmonic $Au_{279}(SR)_{84}$ (where SR = thiolate);[18,19] note that both Au_{246} and Au_{279} are indeed of the same nanometer size (2.2 nm diameter); thus, without precisely controlling the number of atoms, one would not have been able to discover the sharp transition from nonmetallic to metallic state and many other cases of the unique properties of this new class of materials. Such ultrasmall NPs of atomic precision (often called nanoclusters, NCs)[20−23] provide great opportunities for performing unprecedented manipulations, such as the tailoring of the NCs, which may lead to structural alteration and drastic variations in material properties.[24−28]

While a number of stable sizes of $Au_n(SR)_m$ NCs have been reported, they are discontinuous (i.e., only certain magic sizes).[29,30] To fill up the blanks in the "periodic table" of atomically precise NCs, new synthetic strategies are critically needed. The ligand-induced transformation method was quite successful in expanding the size library.[31−35] This method indicates that the sizes/structures of NCs are ligand-dictated, and such a ligand-directing synthesis is applied not only to

Received: August 24, 2020

thiolate-protected Au NCs but also to alkynyl-protected ones.[36−38] Surface tailoring was also reported for controlling the surface structure and the NC properties.[39−41] However, all these works did not lead to any continuous size series in which the core size evolves atom-by-atom with the NCs bearing the same ligand.

The atom-by-atom manipulation is of fundamental importance to understand the size evolution of NCs. In recent work, the Xie group developed a noncrystallization approach to reveal the dynamics of size conversion and single atom diffusion.[42−44] However, the missing crystal structures preclude a deeper understanding of the structural effect of single atom augmentation and structure−property relationships. A delicate design for an atom-by-atom series to reveal the growth mechanism has not been achieved so far, because some strict requirements are yet to be fulfilled: (1) the NCs should be protected by the same ligand; (2) multiple (e.g., more than three) NCs should be related by one (metal) atom increment; and (3) the structures of NCs should be solved by crystallography for correlating the properties with structures. When such a correlated series is achieved, i.e., fixing as many factors as possible (e.g., the ligand type) while changing only one variable (e.g., size, structure), one will be able to achieve much more insightful studies on the evolution of properties by focusing on one factor while decoupling other factors from it.[45−48]

In this work, we report two new NCs, $Au_{22}(SAdm)_{16}$ and $Au_{22}Cd_1(SAdm)_{16}$ (SAdm = adamantanethiolate) with their crystal structures solved. More importantly, $Au_{21}(SAdm)_{15}$ and $Au_{24}(SAdm)_{16}$ NCs are prepared together with $Au_{22}(SAdm)_{16}$, and we found no stable form of $Au_{23}(SAdm)_{16}$, but its bimetallic counterpart $Au_{22}Cd_1(SAdm)_{16}$ does exist. Therefore, atom-by-atom evolution from Au_{21} to Au_{22} to $Au_{22}Cd_1$ (23 metal atoms) to Au_{24} is achieved while keeping the ligand the same. Structurally, a distinct transition is observed by single-Cd atom insertion, i.e., $Au_{22}(SAdm)_{16}$ with a bioctahedral Au_{10} kernel is transformed into $Au_{22}Cd_1(SAdm)_{16}$ with a cuboctahedral $Au_{12}Cd_1$ kernel, and correspondingly, the optical absorption spectra change dramatically. Minimal effects on ionization potential (IP) and electron affinity (EA) were found by density functional theory (DFT) calculations on the series. Overall, the crystallized four SAdm-protected NCs with atom-by-atom size evolution are quite unique and shed light on the growth, structure, and property correlations. The results indicate that continuous metal atom numbers can be accessed in atomically precise NCs.

RESULTS AND DISCUSSION

Syntheses and Crystal Structures. The synthesis of $Au_{22}(SAdm)_{16}$, along with $Au_{21}(SAdm)_{15}$[49] and $Au_{24}(SAdm)_{16}$,[50] followed a common method of reduction of Au^{I}−SAdm by $NaBH_4$. Different NCs were then separated by thin layer chromatography (TLC). No stable form of $Au_{23}(SAdm)_{16}$ was found, but when Au^{I}−SAdm and Cd^{II}−SAdm complexes were coreduced, $Au_{22}Cd_1(SAdm)_{16}$ was obtained (see Supporting Information SI for details, Figure S1−S4) and it is stable. Crystallization of both $Au_{22}(SAdm)_{16}$ and $Au_{22}Cd_1(SAdm)_{16}$ was performed by layer diffusion of methanol into the CH_2Cl_2 solutions of corresponding NCs, followed by X-ray crystallography analysis. The $Au_{21}(SAdm)_{15}$ and $Au_{24}(SAdm)_{16}$ NCs were also purified by crystallization with the same method.

The $Au_{22}(SAdm)_{16}$ structure contains a bioctahedral Au_{10} kernel (Figure 1a), which is surrounded by a large $Au_8(SR)_9$

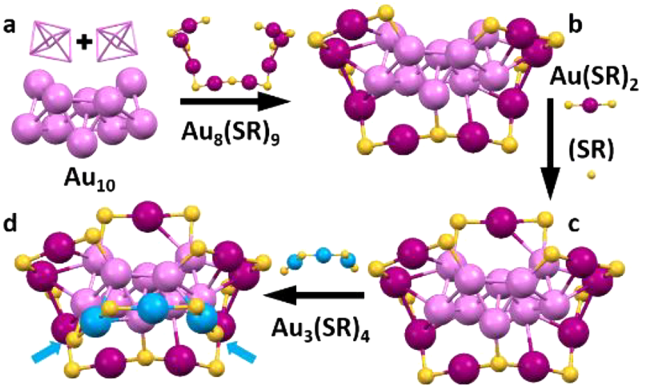

Figure 1. Structural anatomy of $Au_{22}(SAdm)_{16}$. Color codes: violet = kernel Au, magenta/blue = staple Au, and yellow = S.

staple motif (Figure 1b), then a monomeric $Au(SR)_2$ motif on the top and a bridging thiolate in the back (Figure 1c), and finally a trimeric $Au_3(SR)_4$ motif in the front (Figure 1d, with Au atoms highlighted in blue, S atoms binding to the kernel indicated by arrows). The total structure differs from that of $Au_{21}(SAdm)_{15}$ as the front $Au_2(SR)_3$ motif on $Au_{21}(SAdm)_{15}$ (Figure S5)[49] is replaced by a longer $Au_3(SR)_4$ motif in $Au_{22}(SAdm)_{16}$, hence, resulting in a more distorted Au_{10} kernel which expands outward (Figure S6).

The Cd-doped $Au_{23-x}Cd_x(SAdm)_{16}$ NC possesses an average number of Cd of 1.1 determined by X-ray crystallography, very close to the single Cd-doped nanocluster mass peak in the MS spectrum (Figure S2, blue profile); thus, we formulate the product as $Au_{22}Cd_1(SAdm)_{16}$. Its structure contains a cuboctahedral $Au_{12}Cd_1$ kernel in which the Cd atom is distributed primarily at the two C_2 symmetric positions in the kernel (Figure 2a, highlighted in light yellow, occupancies 32−

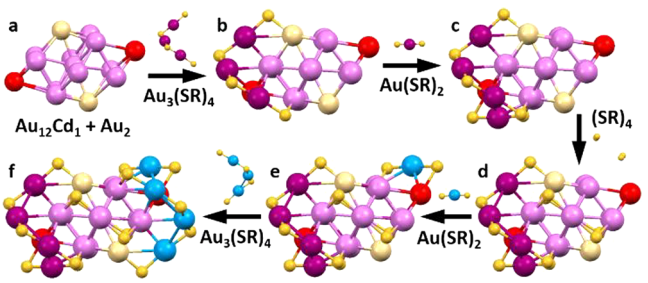

Figure 2. Structural anatomy of $Au_{22}Cd_1(SAdm)_{16}$. Color codes: violet/red = kernel Au, light yellow = kernel Cd/Au, magenta/blue = motif Au, and yellow = S (smaller balls).

39%), with other sites having very low Cd occupancies (<10%, Table S1). We note that for any individual $Au_{22}Cd_1(SAdm)_{16}$ NC, the single Cd atom only resides at one of the sites, rather than all over the sites simultaneously; but all such $Au_{22}Cd_1(SAdm)_{16}$ NCs exist in the macroscopic crystal and give rise to the statistical average of occupancies in the X-ray crystallography analysis. The one Cd atom inside the NC indicates the 23-atom NC requires Cd to provide one more valence electron than Au, i.e., Cd ($5s^2$) vs Au ($6s^1$). The $Au_{12}Cd_1$ kernel is capped by two extra Au atoms on two sides (Figure 2a, highlighted in red), and further protected by two $Au_3(SR)_4$

https://dx.doi.org/10.1021/jacs.0c09110
J. Am. Chem. Soc. XXXX, XXX, XXX−XXX

(Figure 2b/f), two $Au(SR)_2$ (Figure 2c/e) motifs, as well as four bridging thiolates (Figure 2d). Compared to the $Au_{24}(SAdm)_{16}$ structure (Figure S7),[50] although the left-side motifs (highlighted in magenta) of the two NCs are alike, the right-side motifs (highlighted in blue) are different and oppositely arranged, i.e., the $Au_3(SR)_4$ of $Au_{22}Cd_1(SAdm)_{16}$ is in the front (Figure 2f, blue), whereas that of $Au_{24}(SAdm)_{16}$ is at the back (Figure S7).

Note that $[Au_{23}(S\text{-}c\text{-}C_6H_{11})_{16}]^-$,[51] an anionic NC protected by different thiolate ligand (Figure S8), has the same kernel and the same number of staple motifs as $Au_{22}Cd_1(SAdm)_{16}$ here. However, the arrangements of surface motifs are reversed: $[Au_{23}(S\text{-}c\text{-}C_6H_{11})_{16}]^-$ is achiral due to its central symmetry (Figure S8), while $Au_{22}Cd_1(SAdm)_{16}$ is chiral with quasi-C_2 symmetry (Figure S9), indicating that different bonding modes of metal−ligands play a critical role in influencing the surface characteristic features of chirality.

The $Au_{21}(SAdm)_{15}$ and $Au_{24}(SAdm)_{16}$ NCs, which were previously reported,[49,50] are obtained together with $Au_{22}(SAdm)_{16}$ by the new method herein (Figure S1), whereas $Au_{22}Cd_1(SAdm)_{16}$ was prepared by adding a small amount of Cd(II); thus, a unique series of single-atom augment in size, i.e., $Au_{21}(SAdm)_{15}$, $Au_{22}(SAdm)_{16}$, $Au_{22}Cd_1(SAdm)_{16}$, and $Au_{24}(SAdm)_{16}$, is fulfilled. Within this particular series, three major conclusions can be drawn: (1) continuous metal atom numbers (21, 22, 23, and 24) are accessible in atomically precise NCs even with the same ligands; (2) all crystallization can be accomplished at atom-by-atom size evolution; (3) the structural transformation can be triggered by only one atom ($Au_{22}(SAdm)_{16}$ to $Au_{22}Cd_1(SAdm)_{16}$).

To understand the structural transition, we performed the natural bond orbital (NBO) charge analysis (Figure S10). It is clear that the kernels of $Au_{21}(SAdm)_{15}$ and $Au_{22}(SAdm)_{16}$ are positive, while the central Au atom of $Au_{22}Cd_1(SAdm)_{16}$ and also of $Au_{24}(SAdm)_{16}$ are negative. Thus, electron density transfer to the central Au could be a potential reason that triggers the structural transition due to the effects of charge localization on the bond angles.[48]

Optical Absorption and Electronic Structure. The optical properties of NCs is dominated by absorption in the UV−vis spectra due to their small sizes. It is demonstrated herein that with the ligand being kept the same, the addition of metal atoms to the NC in an atom-by-atom manner can cause dramatic changes to the optical absorbance (Figure 3), reflected in a distinct color change in the NC solutions (Figure 3, inset). DFT calculations reveal that the orbitals near the HOMO−LUMO gap (E_g) primarily arise from atomic 6sp orbitals of the kernel Au atoms,[52] i.e., the energy gap is primarily dictated by the kernel. Compared to that of $Au_{21}(SAdm)_{15}$ (E_g = 1.61 eV), the E_g of $Au_{22}(SAdm)_{16}$ (note: both have a similar 10-atom bioctahedral kernel) increases to 1.74 eV upon the addition of Au-SR on the surface (Figure S11). However, the general profiles of the spectra of Au_{21} and Au_{22} are similar due to their related structures. The further addition of one Cd atom to $Au_{22}(SAdm)_{16}$ results in $Au_{22}Cd_1(SAdm)_{16}$ with an $Au_{12}Cd_1$ cuboctahedral kernel and a distinctly different optical spectrum due to the structural transformation (Figure 3). A strong absorption peak at 607 nm was observed, and E_g increases to 1.86 eV (Figure S11). In contrast, although $Au_{24}(SAdm)_{16}$ shares the same cuboctahedral kernel,[50] its experimental HOMO−LUMO gap decreases to 1.52 eV, caused by the insertion of one Au atom between the kernel and the surface motif as well as the rearrangement of the surface structure.

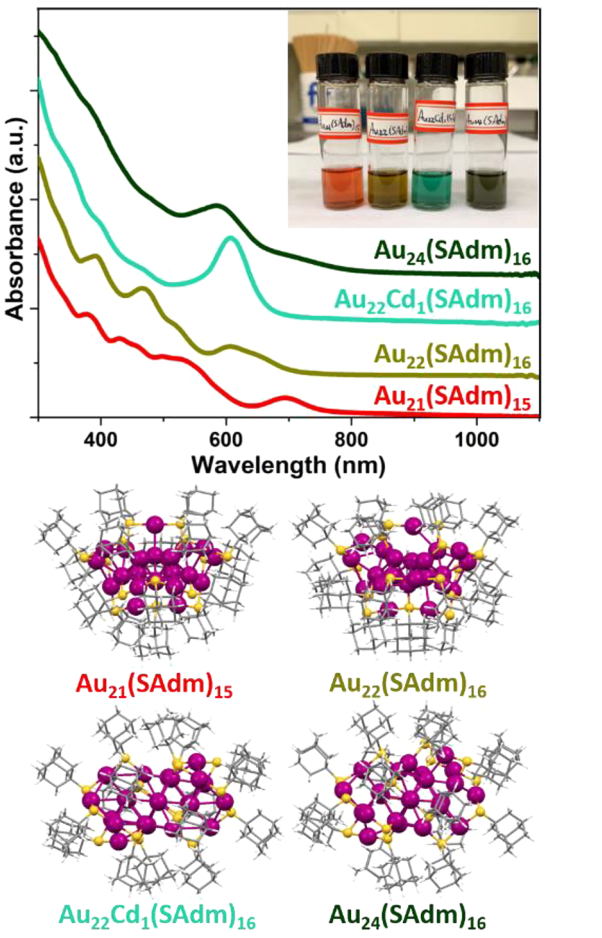

Figure 3. UV−vis spectra of $Au_{21}(SAdm)_{15}$, $Au_{22}(SAdm)_{16}$, $Au_{22}Cd_1(SAdm)_{16}$, and $Au_{24}(SAdm)_{16}$ NCs; inset: photographs of the dichloromethane solutions of the four NCs, from left to right are $Au_{21}(SAdm)_{15}$, $Au_{22}(SAdm)_{16}$, $Au_{22}Cd_1(SAdm)_{16}$, and $Au_{24}(SAdm)_{16}$, respectively.

The successive atom-by-atom manipulation of atomically precise NCs allows one to control the optical absorption, which exhibits high sensitivity to subtle changes in the structure (i.e., from the kernel to the surface), resulting in dramatic color changes in the NC solutions. We further analyzed the NCs' electronic structures. Mulliken contributions are calculated to rationalize atomic-level contributions to the Kohn−Sham (KS) HOMO and LUMO of each NC in the series (Figure 4; Figures S12−S15 contain HOMO−3 to LUMO+3 contributions; see Computational Details section in SI). On the basis of the KS orbital energy level diagrams (Figure S16) and Mulliken contribution diagrams (Figure 4), the LUMOs of all four NCs are very close in energy (with a range of 0.14 eV across the four LUMO energy levels); HOMOs, however, exhibit a larger range of energy levels (i.e., 0.31 eV). Thus, the energy gaps (E_g in Figure 4), which show the same trend as do the experimental spectra (Figure S11), are primarily decided by the HOMOs (which can also be observed in the KS diagrams in Figure S16). In a comparison of $Au_{21}(SAdm)_{15}$ and $Au_{22}(SAdm)_{16}$ having a common Au_{10} kernel, the LUMOs are localized at the central atoms of both NCs (columns 1 and 2 in Figure 4, marked in blue). By contrast, although the contributors to the HOMO spread throughout $Au_{21}(SAdm)_{15}$, those that decide the HOMO of $Au_{22}(SAdm)_{16}$ are localized at one side of the NC (columns 1 and 2 in Figure 4, marked in red). As to $Au_{22}Cd_1(SAdm)_{16}$

https://dx.doi.org/10.1021/jacs.0c09110
J. Am. Chem. Soc. XXXX, XXX, XXX−XXX

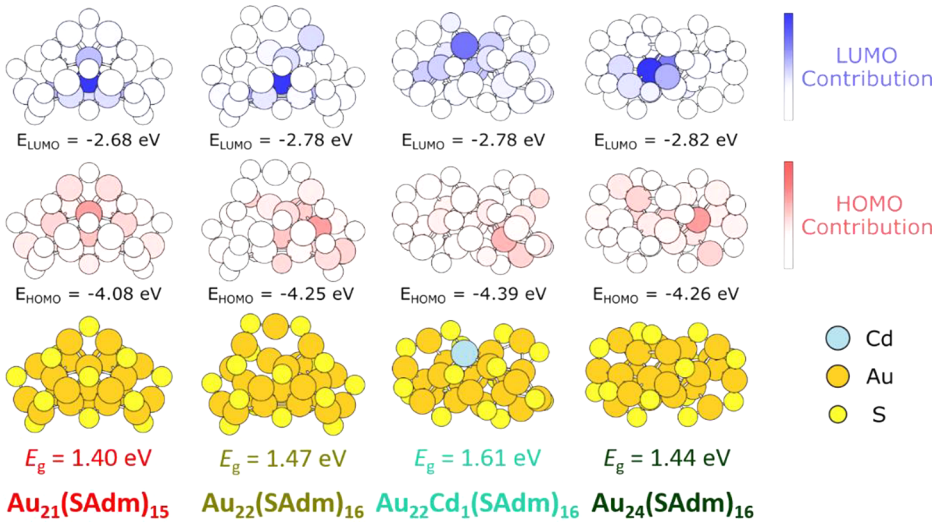

Figure 4. Energy levels and Mulliken contributions by different atoms to the KS HOMO and LUMO in the SAdm-NC series. Darker color (blue for LUMOs and red for HOMOs) corresponds to stronger contribution. R groups (C and H atoms) of SAdm ligands are removed for clarity.

(column 3 in Figure 4), Cd contributes greatly to the LUMO due to its lower electronegativity than Au (χ_{Cd} = 1.69, χ_{Au} = 2.54) as well as its divalent nature (i.e., contributing an additional valence electron to the system). The decrease in the HOMO energy of $Au_{22}Cd_1(SAdm)_{16}$ is related to its cuboctahedral structure. The LUMO of $Au_{24}(SAdm)_{16}$ is localized on one Au atom in the shell site of the Au_{13} kernel, while the atoms contributing to the HOMO involve both the kernel and the surface motif atoms in the NC. Generally, this series of four NCs shows that the atomic contributions to the LUMOs are more concentrated, while the HOMOs are delocalized over more atoms. Thus, the HOMO−LUMO transitions exhibit a charge-localization feature, which is distinctly different than the vast majority of the reported NCs.[20,52]

An interesting issue to address is that the number of valence electron in this series of NCs transits from 6e for both $Au_{21}(SAdm)_{15}$ and $Au_{22}(SAdm)_{16}$ (i.e., 21−15 = 22−16 = 6e) to 8e for both $Au_{22}Cd_1(SAdm)_{16}$ and $Au_{24}(SAdm)_{16}$ (22 + 2−16 = 24−16 = 8e) but skips the 7e case. Experimental efforts to synthesize the 7e $Au_{23}(SAdm)_{16}$ by adjusting the synthetic conditions were not successful, and only when Cd(II) was used, could a 23-atom NC be obtained. In a previous periodic series (i.e., $Au_{28}(SR)_{20}$, $Au_{36}(SR)_{24}$, $Au_{44}(SR)_{28}$ and $Au_{52}(SR)_{32}$, where SR = *tert*-butyl-benzenethiolate), the free electron number increased from 8e, 12e, 16e to 20e with the same interval (4e):[46] the same 4e increment for the series of $Au_{28}(SR)_{20}$, $Au_{34}(SR)_{22}$, $Au_{42}(SR)_{26}$ (SR = cyclohexanethiolate).[47] Note that in another series reported previously,[48] as more Ag atoms were doped into the kernel, the 6e $Au_{20}Ag_1(SAdm)_{15}$ also transited to the 8e $Au_{19}Ag_4(SAdm)_{15}$. The results of the new SAdm-protected series in the current work suggest that an even number of valence electrons is required,[53] even in the atom-by-atom growth.

Electronic Stability. Due to the distinct feature of atom-by-atom size evolution, this series becomes an ideal model to study the electronic structure-related stability of atomically precise NCs. Moreover, determining the explicit electronic properties is important for photophysical and photochemical applications.[54−57] Critical parameters such as IP and EA are decisive to electronic properties, especially for the applications of NPs in photovoltaics and photocatalysis.[54−56] In recent work, it was found that both IP and EA of magic-sized $Au_n(SR)_m$ NCs (n = 18 to 279) trend with the number of Au (linearly with $n^{-1/3}$),[58] in which IP decreases (less positive) and EA increases (more negative) as the NC size goes up, indicating a general size-dependent electronic properties for atomically precise NCs, which is akin to elements in the periodic table; whether the electronic properties would behave similarly within an atom-by-atom evolution remains unknown.

In contrast to elements in the same period in the Periodic Table, there is little change in IP and EA of the series of four NCs (ΔIP ≤ 6.2 kcal/mol, ΔEA ≤ 3.5 kcal/mol, Table S2, Figure 5,

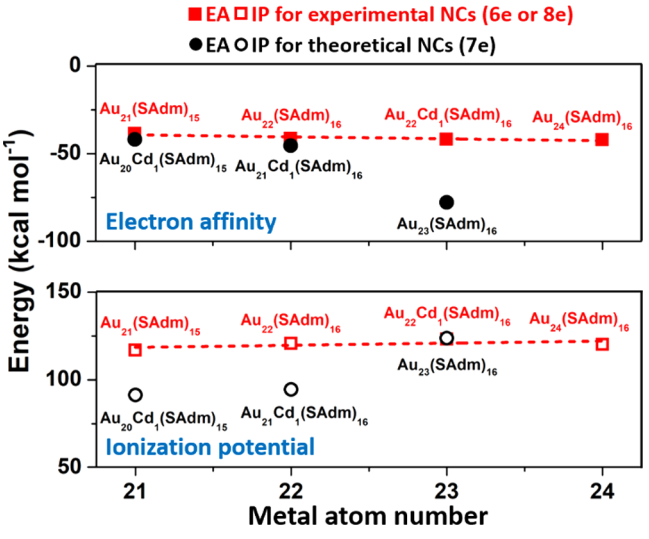

Figure 5. IP and EA as a function of metal atom number in NCs. Dashed lines drawn as guides to highlight the little change in IP and EA of the experimental Au_{21}, Au_{22}, $Au_{22}Cd_1$, and Au_{24} NCs.

solid/open red squares), indicating size-agnostic electronic properties for the $Au_{21} - Au_{22} - Au_{22}Cd_1 - Au_{24}$ series. In other words, the energy to remove an electron from these NCs is similar, and the affinity of these NCs to receive an electron is also almost the same. Note that no 7e NC is present in this atom-by-atom series of NCs; the 23-metal-atom NC requires one Cd to

https://dx.doi.org/10.1021/jacs.0c09110
J. Am. Chem. Soc. XXXX, XXX, XXX−XXX

be doped so as to have an extra valence electron (Cd ($5s^2$) vs Au ($6s^1$)). According to the electronic counting rules,[59,60] odd numbers of valence electrons are not favored except for the icosahedral NCs.[61−63]

The atom-by-atom series provides an opportunity to understand why 7e Au-SAdm NCs are experimentally not achieved. In order to simulate neutral 7e NCs, a valence electron is removed from $Au_{22}Cd_1(SAdm)_{16}$ by replacing Cd with Au, and a valence electron is added to $Au_{21}(SAdm)_{15}$ and $Au_{22}(SAdm)_{16}$ by replacing an Au with Cd. Thus, three hypotheoretical 7e NCs, $Au_{20}Cd_1(SAdm)_{15}$, $Au_{21}Cd_1(SAdm)_{16}$, and $Au_{23}(SAdm)_{16}$ (all being neutral) are designed (Figure S17) and their electronic properties (IP and EA) are probed with DFT calculations (Table S2). The EAs of the hypotheoretical $Au_{20}Cd_1(SAdm)_{15}$ and $Au_{21}Cd_1(SAdm)_{16}$ follow the trend of the stable NCs (Figure 5, solid black circles), but their IPs deviate and have much lower energy compared to their 6e counterparts (Figure 5, open black circles). These results indicate that the hypotheoretical 7e NCs do not intend to take in an electron to fulfill 8e shell closure but prefer to lose an electron and achieve the same configuration as their stable NC counterparts. The hypotheoretical $Au_{23}(SAdm)_{16}$ NC (neutral) shows an almost identical IP as the stable $Au_{22}Cd_1(SAdm)_{16}$ but a much lower EA than its 8e counterpart, proving that an additional electron is desired by the 23-Au-atom NC. Note that we also did the same calculation on hypotheoretical 8e $[Au_{23}(SAdm)_{16}]^-$, but due to the imbalance between protons and electrons for the anionic cluster, the values are much-deviated (Table S2).

In the given size range of our stable NC series, the IP and EA properties experience minimal size effects. The results agree with previously determined NC structure−property relationships for IP and EA (Figure S18),[58] supporting the use of these models as stability metrics for neutral Au-SR NCs. Furthermore, probing hypotheoretical 7e NCs through Cd−Au replacement reveals that the IP and EA models can distinguish NC stability for heterometal-doped NCs. We note that for the hypotheoretical $Au_{20}Cd_1(SAdm)_{15}$ and $Au_{21}Cd_1(SAdm)_{16}$, Cd is substituted into the Au position that contributes the most to the LUMO of each monometallic NC (columns 1 and 2 in Figure 4, the atoms marked in deep blue) since an additional valence electron is being added to each system. However, since IP and EA are each a cumulative response by the NCs (charges are delocalized), Cd placement should have little effect on these properties. This is confirmed by analyzing a second hypotheoretical $Au_{20}Cd_1(SAdm)_{15}$ NC (labeled with *, Figure S17) whose Cd atom replaces an Au atom that does not contribute to the LUMO of the monometallic system. As Table S2 shows, there is little difference in IP and EA between these hypotheoretical NC isomers. In summary, the results reveal that the NC size (number of metal atoms) and the valence electron count dictate the IP and EA trends for the stability of neutral NCs.

The above analysis from the IP and EA demonstrates why 7e NCs cannot be experimentally accessed. Note that 7e $Au_{25}(SR)_{18}$ was previously synthesized by oxidation of its anionic 8e counterpart, due to the superatomic electronic structure of the NC.[64] However, this is not the case in our NC series. Taking a step further, we can connect the IP and EA analysis to our experimental observations to rationalize why a structural transition occurs between $Au_{22}(SAdm)_{16}$ and $Au_{22}Cd_1(SAdm)_{16}$. First, we note that the $Au_{21}(SAdm)_{15}$, $Au_{22}(SAdm)_{16}$, and $Au_{24}(SAdm)_{16}$ are prepared together and could not be synthesized with a Cd dopant. This is important to show that the structural transition within this series is in part due to size effects (the cuboctahedral kernel is preferred over bioctahedral above 22 metal atoms). In addition, the 23-atom NC could only be formed through heterometal doping ($Au_{23}(SAdm)_{16}$ was found to be unstable), resulting in only 6e and 8e NCs observed in experiments. Although other Au-SR compositions could potentially exist within this size regime (e.g., 6e $Au_{23}(SAdm)_{17}$), the synthesis results have not proved that. Therefore, our collective results show that the structural transition from $Au_{22}(SAdm)_{16}$ to $Au_{22}Cd_1(SAdm)_{16}$ is driven by size and a stabilizing electron shell closure through Cd doping. Overall, this series of NCs provides insights into the atom-by-atom growth of NCs, which is intriguing in nanocluster research on nucleation and growth.[65−67]

Electron Dynamics. We further carried out nanosecond (ns) transient absorption (TA) measurements (λ_{ex} = 400 nm) to probe the electron dynamics in this atom-by-atom series (Figure 6a−d), and very different excited state dynamics were observed

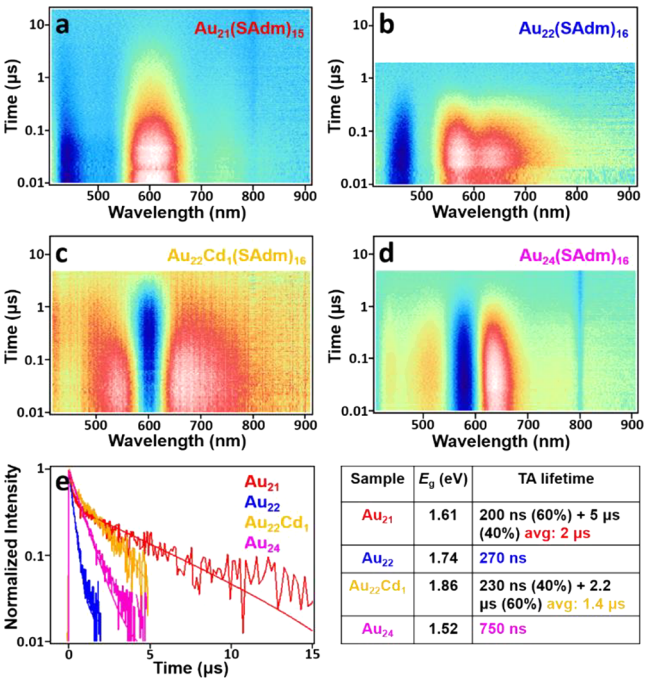

Figure 6. ns-TA data maps of (a) $Au_{21}(SAdm)_{15}$, (b) $Au_{22}(SAdm)_{16}$, (c) $Au_{22}Cd_1(SAdm)_{16}$, and (d) $Au_{24}(SAdm)_{16}$ NCs. (e) Kinetic traces and corresponding fits with excitation of 400 nm for the four NCs.

(Figure 6e). Specifically, single exponential decay lifetimes (τ) of 270 and 750 ns are found for $Au_{22}(SAdm)_{16}$ and $Au_{24}(SAdm)_{16}$, respectively; whereas two-component lifetimes are detected for $Au_{21}(SAdm)_{15}$ (60% 200 ns and 40% 5 μs with avg. τ = 2 μs) and $Au_{22}Cd_1(SAdm)_{16}$ (40% 230 ns and 60% 2.2 μs with avg. τ = 1.4 μs).

It is surprising to see that the largest difference is found between $Au_{21}(SAdm)_{15}$ and $Au_{22}(SAdm)_{16}$, which actually exhibit similar structures (e.g., common Au_{10} kernel); in addition, the E_g of $Au_{22}(SAdm)_{16}$ (~1.74 eV) is actually larger than that of $Au_{21}(SAdm)_{15}$ (~1.61 eV) and one would expect a slower relaxation according to the energy gap law, but $Au_{21}(SAdm)_{15}$ instead exhibits a much longer (~10 times) average carrier lifetime. Generally, the carrier lifetime is sensitive to the structure when the NCs are in the small size regime (e.g., the number of Au atoms <50); for instance, a drastic variation of

https://dx.doi.org/10.1021/jacs.0c09110
J. Am. Chem. Soc. XXXX, XXX, XXX−XXX

more than 3 orders of magnitude was observed between $Au_{30}(SAdm)_{18}$ and $Au_{38}S_2(SAdm)_{20}$ which have comparable E_g.[68] The NC series with face-centered cubic (fcc) kernels, i.e., $Au_{36}(SR)_{24}$, $Au_{44}(SR)_{28}$, and $Au_{52}(SR)_{32}$ with comparable E_g, demonstrates comparable lifetimes (100−200 ns).[65] In the comparison of carrier lifetimes between Au_{21} and Au_{22}, the short components of Au_{21} (200 ns) and Au_{22} (270 ns) are on the same scale and should be related to their similar kernel structure, while the long component (5 μs) of Au_{21} could originate from a slow decay channel modulated by the surface motif structure. The $Au_{22}Cd_1(SAdm)_{16}$ NC also has two lifetime components, and the short component (230 ns) is similar to those of Au_{21} and Au_{22} NCs. The average lifetime (1.4 μs) of $Au_{22}Cd_1(SAdm)_{16}$ is twice that of $Au_{24}(SAdm)_{16}$ due to Cd-doping and the missing of one Au atom on the surface. From the excited state lifetimes of the NC series, one sees that the excited state relaxation of small sized Au NCs is very sensitive to the structure of both the kernel and surface motifs.

Unlike the nanosecond dynamics, the femtosecond dynamics of this series of NCs can be divided by their structures: Au_{21} and Au_{22} form a group that shares similar ultrafast dynamics, while $Au_{22}Cd_1$ and Au_{24} form a second group with similar dynamics (Figure S19). Moreover, the ultrafast dynamics is strongly related to their HOMO−LUMO gaps. In the initial 1−2 ps, the hot electrons with energy higher than the HOMO−LUMO gap experience cooling to the lowest excited state (Figure S19). One can observe that with the same pump energy at 3.1 eV (400 nm), the cooling time increases as the HOMO−LUMO gap decreases. On the basis of Mulliken contributions obtained from DFT calculation, the LUMOs of the four NCs are concentrated while the LUMO+n states are delocalized. Therefore, the fast cooling should also be accompanied by e-localization process in the NC series.

CONCLUSION

All crystallization is realized for an atom-by-atom size evolving series of NCs, i.e., $Au_{21}(SAdm)_{15}$, $Au_{22}(SAdm)_{16}$, $Au_{22}Cd_1(SAdm)_{16}$, and $Au_{24}(SAdm)_{16}$, and three important conclusions can be drawn: (1) atomically precise NCs with continuous metal atom numbers can be achieved even when protected by the same ligand; (2) correlated NCs with atom-by-atom size evolution can be crystallized to reveal the growth mechanism; (3) merely one Cd atom can trigger the structural transformation from $Au_{22}(SAdm)_{16}$ with bioctahedral Au_{10} kernel to $Au_{22}Cd_1(SAdm)_{16}$ with cuboctahedral $Au_{12}Cd_1$ kernel. Moreover, various properties of this series, including optical absorbance, carrier lifetime, as well as the calculated KS diagrams, IP and EA, are compared to obtain the single-atom increment effects. A structure transition is observed in the series of NCs. The optical properties and excited state dynamics exhibit high sensitivity to the structure; whereas IP and EA are similar among the four sizes, indicating that cumulative electronic properties experience little effect. By alternating Au−Cd in the series, hypotheoretical 7e NCs are also simulated of which the electronic properties deviate from previously established structure−property relationships, rationalizing the lack of stability in 7e NCs and their absence in this NC series. Future work on atom-by-atom manipulations is expected to reveal more insights into the fundamental properties of metal NCs.

ASSOCIATED CONTENT

Supporting Information

The Supporting Information is available free of charge at https://pubs.acs.org/doi/10.1021/jacs.0c09110.

Details of synthesis, characterizations, including UV−vis, MS, ESI-MS spectra, X-ray crystallography, TA analysis, computational details, and KS orbital analysis (PDF)

Crystallographic structures of $Au_{22}(SAdm)_{16}$ (CIF)

Crystallographic structures of $Au_{23-x}Cd_x(SAdm)_{16}$ (CIF)

AUTHOR INFORMATION

Corresponding Authors

Giannis Mpourmpakis − *Department of Chemical Engineering, University of Pittsburgh, Pittsburgh, Pennsylvania 15261, United States;* orcid.org/0000-0002-3063-0607; Email: gmpourmp@pitt.edu

Rongchao Jin − *Department of Chemistry, Carnegie Mellon University, Pittsburgh, Pennsylvania 15213, United States;* orcid.org/0000-0002-2525-8345; Email: rongchao@andrew.cmu.edu

Authors

Yingwei Li − *Department of Chemistry, Carnegie Mellon University, Pittsburgh, Pennsylvania 15213, United States;* orcid.org/0000-0002-4813-6009

Michael J. Cowan − *Department of Chemical Engineering, University of Pittsburgh, Pittsburgh, Pennsylvania 15261, United States;* orcid.org/0000-0001-8706-782X

Meng Zhou − *Department of Physics, University of Miami, Coral Gables, Florida 33146, United States;* orcid.org/0000-0001-5187-9084

Tian-Yi Luo − *Department of Chemistry, University of Pittsburgh, Pittsburgh, Pennsylvania 15260, United States;* orcid.org/0000-0002-9973-9328

Yongbo Song − *Department of Chemistry, Carnegie Mellon University, Pittsburgh, Pennsylvania 15213, United States*

He Wang − *Department of Physics, University of Miami, Coral Gables, Florida 33146, United States;* orcid.org/0000-0003-1365-0304

Nathaniel L. Rosi − *Department of Chemistry, University of Pittsburgh, Pittsburgh, Pennsylvania 15260, United States;* orcid.org/0000-0001-8025-8906

Complete contact information is available at: https://pubs.acs.org/10.1021/jacs.0c09110

Author Contributions

[$]These authors contributed equally.

Funding

R.J. acknowledges financial support from the National Science Foundation (NSF) under Grant No. DMR-1808675. G.M. acknowledges financial support from NSF, CBET-CAREER program, under Grant No. 1652694. H.W. acknowledges financial support by the Air Force Office of Scientific Research (AFOSR) Award FA9550−17−1−0099.

Notes

The authors declare no competing financial interest.

ACKNOWLEDGMENTS

Computational support was provided by the Center for Research Computing (CRC) at the University of Pittsburgh, as well as, the Extreme Science and Engineering Discovery

Environment (XSEDE), which is supported by the NSF (ACI-1548562). We acknowledge Rosalba Juarez-Mosqueda from Department of Chemical Engineering, University of Pittsburgh, for performing preliminary DFT calculations on the NC series.

REFERENCES

(1) Stroscio, J. A.; Celotta, R. J. Controlling the Dynamics of a Single Atom in Lateral Atom Manipulation. *Science* **2004**, *306*, 242−247.
(2) Suenaga, K.; Koshino, M. Atom-by-Atom Spectroscopy at Graphene Edge. *Nature* **2010**, *468*, 1088−1090.
(3) Kitchen, D.; Richardella, A.; Tang, J.-M.; Flatté, M. E.; Yazdani, A. Atom-by-Atom Substitution of Mn in GaAs and Visualization of Their Hole-Mediated Interactions. *Nature* **2006**, *442*, 436−439.
(4) Higaki, T.; Li, Q.; Zhou, M.; Zhao, S.; Li, Y.; Li, S.; Jin, R. Toward the Tailoring Chemistry of Metal Nanoclusters for Enhancing Functionalities. *Acc. Chem. Res.* **2018**, *51*, 2764−2773.
(5) Fernando, A.; Weerawardene, K. L. D. M.; Karimova, N. V.; Aikens, C. M. Quantum Mechanical Studies of Large Metal, Metal Oxide, and Metal Chalcogenide Nanoparticles and Clusters. *Chem. Rev.* **2015**, *115*, 6112−6216.
(6) Guan, Z. J.; Hu, F.; Li, J.-J.; Liu, Z.-R.; Wang, Q.-M. Homoleptic Alkynyl-Protected Gold Nanoclusters with Unusual Compositions and Structures. *Nanoscale* **2020**, *12*, 13346−13350.
(7) Yang, H.; Yan, J.; Wang, Y.; Deng, G.; Su, H.; Zhao, X.; Xu, C.; Teo, B. K.; Zheng, N. From Racemic Metal Nanoparticles to Optically Pure Enantiomers in One Pot. *J. Am. Chem. Soc.* **2017**, *139*, 16113−16116.
(8) Tasaka, Y.; Nakamura, K.; Malola, S.; Hirata, K.; Kim, K.; Koyasu, K.; Häkkinen, H.; Tsukuda, T. Electron Binding in a Superatom with a Repulsive Coulomb Barrier: The Case of $[Ag_{44}(SC_6H_3F_2)_{30}]^{4-}$ in the Gas Phase. *J. Phys. Chem. Lett.* **2020**, *11*, 3069−3074.
(9) Wu, Z.; Yao, Q.; Zang, S.; Xie, J. Directed Self-Assembly of Ultrasmall Metal Nanoclusters. *ACS. Mater. Lett.* **2019**, *1*, 237−248.
(10) Konishi, K.; Iwasaki, M.; Shichibu, Y. Phosphine-Ligated Gold Clusters with Core+exo Geometries: Unique Properties and Interactions at the Ligand-Cluster Interface. *Acc. Chem. Res.* **2018**, *51*, 3125−3133.
(11) Niihori, Y.; Koyama, Y.; Watanabe, S.; Hashimoto, S.; Hossain, S.; Nair, L. V.; Kumar, B.; Kurashige, W.; Negishi, Y. Atomic and Isomeric Separation of Thiolate-Protected Alloy Clusters. *J. Phys. Chem. Lett.* **2018**, *9*, 4930−4934.
(12) Bhattarai, B.; Zaker, Y.; Atnagulov, A.; Yoon, B.; Landman, U.; Bigioni, T. P. Chemistry and Structure of Silver Molecular Nanoparticles. *Acc. Chem. Res.* **2018**, *51*, 3104−3113.
(13) Cook, A. W.; Hayton, T. W. Case Studies in Nanocluster Synthesis and Characterization: Challenges and Opportunities. *Acc. Chem. Res.* **2018**, *51*, 2456−2464.
(14) Gan, Z.; Xia, N.; Wu, Z. Discovery, Mechanism, and Application of Antigalvanic Reaction. *Acc. Chem. Res.* **2018**, *51*, 2774−2783.
(15) Sharma, S.; Chakrahari, K. K.; Saillard, J.-Y.; Liu, C. W. Structurally Precise Dichalcogenolate-Protected Copper and Silver Superatomic Nanoclusters and Their Alloys. *Acc. Chem. Res.* **2018**, *51*, 2475−2483.
(16) Ghosh, A.; Mohammed, O. F.; Bakr, O. M. Atomic-Level Doping of Metal Clusters. *Acc. Chem. Res.* **2018**, *51*, 3094−3103.
(17) Katla, S. K.; Zhang, J.; Castro, E.; Bernal, R. A.; Li, X. Atomically Precise $Au_{25}(SG)_{18}$ Nanoclusters: Rapid Single-Step Synthesis and Application in Photothermal Therapy. *ACS Appl. Mater. Interfaces* **2018**, *10*, 75−82.
(18) Zeng, C.; Chen, Y.; Kirschbaum, K.; Lambright, K. J.; Jin, R. Emergence of Hierarchical Structural Complexities in Nanoparticles and Their Assembly. *Science* **2016**, *354*, 1580−1584.
(19) Higaki, T.; Zhou, M.; Lambright, K. J.; Kirschbaum, K.; Sfeir, M. Y.; Jin, R. Sharp Transition from Nonmetallic Au_{246} to Metallic Au_{279} with Nascent Surface Plasmon Resonance. *J. Am. Chem. Soc.* **2018**, *140*, 5691−5695.
(20) Jin, R.; Zeng, C.; Zhou, M.; Chen, Y. Atomically Precise Colloidal Metal Nanoclusters and Nanoparticles: Fundamentals and Opportunities. *Chem. Rev.* **2016**, *116*, 10346−10413.
(21) Chakraborty, I.; Pradeep, T. Atomically Precise Clusters of Noble Metals: Emerging Link between Atoms and Nanoparticles. *Chem. Rev.* **2017**, *117*, 8208−8271.
(22) Lei, Z.; Wan, X.-K.; Yuan, S.-F.; Guan, Z.-J.; Wang, Q.-M. Alkynyl Approach toward the Protection of Metal Nanoclusters. *Acc. Chem. Res.* **2018**, *51*, 2465−2474.
(23) Yan, J.; Teo, B. K.; Zheng, N. Surface Chemistry of Atomically Precise Coinage-Metal Nanoclusters: From Structural Control to Surface Reactivity and Catalysis. *Acc. Chem. Res.* **2018**, *51*, 3084−3093.
(24) Li, H.; Zhai, H.; Zhou, C.; Song, Y.; Ke, F.; Xu, W. W.; Zhu, M. Atomically Precise Copper Cluster with Intensely Near-Infrared Luminescence and Its Mechanism. *J. Phys. Chem. Lett.* **2020**, *11*, 4891−4896.
(25) Higaki, T.; Li, Y.; Zhao, S.; Li, Q.; Li, S.; Du, X.-S.; Yang, S.; Chai, J.; Jin, R. Atomically Tailored Gold Nanoclusters for Catalytic Application. *Angew. Chem., Int. Ed.* **2019**, *58*, 8291−8302.
(26) Kang, X.; Zhu, M. Tailoring the Photoluminescence of Atomically Precise Nanoclusters. *Chem. Soc. Rev.* **2019**, *48*, 2422−2457.
(27) Li, Y.; Higaki, T.; Du, X.; Jin, R. Chirality and Surface Bonding Correlation in Atomically Precise Metal Nanoclusters. *Adv. Mater.* **2020**, *32*, 1905488.
(28) Li, Y.; Cowan, M. J.; Zhou, M.; Taylor, M. G.; Wang, H.; Song, Y.; Mpourmpakis, G.; Jin, R. Increasing the Dipole Moments of M_{23} (M = Au/Ag/Cd) Nanoclusters by Heterometal-Doping. *ACS Nano* **2020**, *14*, 6599−6606.
(29) Jin, R. Atomically Precise Metal Nanoclusters: Stable Sizes and Optical Properties. *Nanoscale* **2015**, *7*, 1549−1565.
(30) Negishi, Y.; Nobusada, K.; Tsukuda, T. Glutathione-Protected Gold Clusters Revisited: Bridging the Gap between Gold(I)-Thiolate Complexes and Thiolate-Protected Gold Nanocrystals. *J. Am. Chem. Soc.* **2005**, *127*, 5261−5270.
(31) Zeng, C.; Liu, C.; Pei, Y.; Jin, R. Thiol Ligand-Induced Transformation of $Au_{38}(SC_2H_4Ph)_{24}$ to $Au_{36}(SPh\text{-}t\text{-}Bu)_{24}$. *ACS Nano* **2013**, *7*, 6138−6145.
(32) Zeng, C.; Li, T.; Das, A.; Rosi, N. L.; Jin, R. Chiral Structure of Thiolate-Protected 28-Gold-Atom Nanocluster Determined by X-Ray Crystallography. *J. Am. Chem. Soc.* **2013**, *135*, 10011−10013.
(33) Maman, M. P.; Nair, A. S.; Cheraparambil, H.; Pathak, B.; Mandal, S. Size Evolution Dynamics of Gold Nanoclusters at an Atom-Precision Level: Ligand Exchange, Growth Mechanism, Electrochemical, and Photophysical Properties. *J. Phys. Chem. Lett.* **2020**, *11*, 1781−1788.
(34) Dong, H.; Liao, L.; Wu, Z. Two-Way Transformation between fcc- and Nonfcc-Structured Gold Nanoclusters. *J. Phys. Chem. Lett.* **2017**, *8*, 5338−5343.
(35) Yang, S.; Chen, S.; Xiong, L.; Liu, C.; Yu, H.; Wang, S.; Rosi, N. L.; Pei, Y.; Zhu, M. Total Structure Determination of $Au_{16}(S\text{-}Adm)_{12}$ and $Cd_1Au_{14}(S^tBu)_{12}$ and Implications for the Structure of $Au_{15}(SR)_{13}$. *J. Am. Chem. Soc.* **2018**, *140*, 10988−10994.
(36) Wan, X.-K.; Yuan, S.-F.; Tang, Q.; Jiang, D. -e.; Wang, Q.-M. Alkynyl-Protected Au_{23} Nanocluster: A 12-Electron System. *Angew. Chem., Int. Ed.* **2015**, *54*, 5977−5980.
(37) Wan, X.-K.; Xu, W. W.; Yuan, S.-F.; Gao, Y.; Zeng, X.-C.; Wang, Q.-M. A Near-Infrared-Emissive Alkynyl-Protected Au_{24} Nanocluster. *Angew. Chem., Int. Ed.* **2015**, *54*, 9683−9686.
(38) Li, J.-J.; Guan, Z.-J.; Lei, Z.; Hu, F.; Wang, Q.-M. Same Magic Number but Different Arrangement: Alkynyl-Protected Au_{25} with D_3 Symmetry. *Angew. Chem., Int. Ed.* **2019**, *58*, 1083−1087.
(39) Yang, H.; Wang, Y.; Yan, J.; Chen, X.; Zhang, X.; Häkkinen, H.; Zheng, N. Structural Evolution of Atomically Precise Thiolated Bimetallic $[Au_{12+n}Cu_{32}(SR)_{30+n}]^{4-}$ (n = 0, 2, 4, 6) Nanoclusters. *J. Am. Chem. Soc.* **2014**, *136*, 7197−7200.
(40) Yao, C.; Chen, J.; Li, M.-B.; Liu, L.; Yang, J.; Wu, Z. Adding Two Active Silver Atoms on Au_{25} Nanoparticle. *Nano Lett.* **2015**, *15*, 1281−1287.

https://dx.doi.org/10.1021/jacs.0c09110
J. Am. Chem. Soc. XXXX, XXX, XXX−XXX

(41) Li, Q.; Luo, T.-Y.; Taylor, M. G.; Wang, S.; Zhu, X.; Song, Y.; Mpourmpakis, G.; Rosi, N. L.; Jin, R. Molecular "Surgery" on a 23-Gold-Atom Nanoparticle. *Sci. Adv.* **2017**, *3*, e1603193.
(42) Yao, Q.; Yuan, X.; Fung, V.; Yu, Y.; Leong, D. T.; Jiang, D.; Xie, J. Understanding Seed-Mediated Growth of Gold Nanoclusters at Molecular Level. *Nat. Commun.* **2017**, *8*, 927.
(43) Yao, Q.; Fung, V.; Sun, C.; Huang, S.; Chen, T.; Jiang, D.; Lee, J. Y.; Xie, J. Revealing Isoelectronic Size Conversion Dynamics of Metal Nanoclusters by a Noncrystallization Approach. *Nat. Commun.* **2018**, *9*, 1979.
(44) Zheng, K.; Fung, V.; Yuan, X.; Jiang, D.; Xie, J. Real Time Monitoring of the Dynamic Intracluster Diffusion of Single Gold Atoms into Silver Nanoclusters. *J. Am. Chem. Soc.* **2019**, *141*, 18977−18983.
(45) Zhou, M.; Zeng, C.; Chen, Y.; Zhao, S.; Sfeir, M. Y.; Zhu, M.; Jin, R. Evolution from the Plasmon to Exciton State in Ligand-Protected Atomically Precise Gold Nanoparticles. *Nat. Commun.* **2016**, *7*, 13240.
(46) Zeng, C.; Chen, Y.; Iida, K.; Nobusada, K.; Kirschbaum, K.; Lambright, K. J.; Jin, R. Gold Quantum Boxes: On the Periodicities and the Quantum Confinement in the Au_{28}, Au_{36}, Au_{44}, and Au_{52} Magic Series. *J. Am. Chem. Soc.* **2016**, *138*, 3950−3953.
(47) Dong, H.; Liao, L.; Zhuang, S.; Yao, C.; Chen, J.; Tian, S.; Zhu, M.; Liu, X.; Li, L.; Wu, Z. A Novel Double-Helical-Kernel Evolution Pattern of Gold Nanoclusters: Alternate Single-Stranded Growth at Both Ends. *Nanoscale* **2017**, *9*, 3742−3746.
(48) Li, Y.; Luo, T.-Y.; Zhou, M.; Song, Y.; Rosi, N. L.; Jin, R. A Correlated Series of Au/Ag Nanoclusters Revealing the Evolutionary Patterns of Asymmetric Ag Doping. *J. Am. Chem. Soc.* **2018**, *140*, 14235−14243.
(49) Chen, S.; Xiong, L.; Wang, S.; Ma, Z.; Jin, S.; Sheng, H.; Pei, Y.; Zhu, M. Total Structure Determination of $Au_{21}(S\text{-}Adm)_{15}$ and Geometrical/Electronic Structure Evolution of Thiolate Gold Nanoclusters. *J. Am. Chem. Soc.* **2016**, *138*, 10754−10757.
(50) Crasto, D.; Barcaro, G.; Stener, M.; Sementa, L.; Fortunelli, A.; Dass, A. $Au_{24}(SAdm)_{16}$ Nanomolecules: X-Ray Crystal Structure, Theoretical Analysis, Adaptability of Adamantane Ligands to Form $Au_{23}(SAdm)_{16}$ and $Au_{25}(SAdm)_{16}$, and Its Relation to $Au_{25}(SR)_{18}$. *J. Am. Chem. Soc.* **2014**, *136*, 14933−14940.
(51) Das, A.; Li, T.; Nobusada, K.; Zeng, C.; Rosi, N. L.; Jin, R. Nonsuperatomic $[Au_{23}(SC_6H_{11})_{16}]^-$ Nanocluster Featuring Bipyramidal Au_{15} Kernel and Trimeric $Au_3(SR)_4$ Motif. *J. Am. Chem. Soc.* **2013**, *135*, 18264−18267.
(52) Aikens, C. M. Electronic and Geometric Structure, Optical Properties, and Excited State Behavior in Atomically Precise Thiolate-Stabilized Noble Metal Nanoclusters. *Acc. Chem. Res.* **2018**, *51*, 3065−3073.
(53) Luo, Z.; Nachammai, V.; Zhang, B.; Yan, N.; Leong, D. T.; Jiang, D.; Xie, J. Toward Understanding the Growth Mechanism: Tracing All Stable Intermediate Species from Reduction of Au(I)-Thiolate Complexes to Evolution of Au_{25} Nanoclusters. *J. Am. Chem. Soc.* **2014**, *136*, 10577−10580.
(54) Stamplecoskie, K. G.; Yousefalizadeh, G.; Gozdzialski, L.; Ramsay, H. Photovoltaics as an Experimental Tool for Determining Frontier Orbital Energies and Photocatalytic Activity of Thiol Protected Gold Clusters. *J. Phys. Chem. C* **2018**, *122*, 13738−13744.
(55) Abbas, M. A.; Khan, R.; Yoon, S. J.; Bang, J. H. Role of Regeneration of Nanoclusters in Dictating the Power Conversion Efficiency of Metal-Nanocluster-Sensitized Solar Cells. *ACS Appl. Mater. Interfaces* **2020**, *12*, 16566−16575.
(56) Li, Z.; Liu, C.; Abroshan, H.; Kauffman, D. R.; Li, G. $Au_{38}S_2(SAdm)_{20}$ Photocatalyst for One-Step Selective Aerobic Oxidations. *ACS Catal.* **2017**, *7*, 3368−3374.
(57) Kim, K.; Hirata, K.; Nakamura, K.; Kitazawa, H.; Hayashi, S.; Koyasu, K.; Tsukuda, T. Elucidating the Doping Effect on the Electronic Structure of Thiolate-Protected Silver Superatoms by Photoelectron Spectroscopy. *Angew. Chem., Int. Ed.* **2019**, *58*, 11637−11641.
(58) Cowan, M. J.; Mpourmpakis, G. Structure-Property Relationships on Thiolate-Protected Gold Nanoclusters. *Nanoscale Adv.* **2019**, *1*, 184−188.
(59) Xu, W. W.; Zeng, X. C.; Gao, Y. Application of Electronic Counting Rules for Ligand-Protected Gold Nanoclusters. *Acc. Chem. Res.* **2018**, *51*, 2739−2747.
(60) Pei, Y.; Wang, P.; Ma, Z.; Xiong, L. Growth-Rule-Guided Structural Exploration of Thiolate-Protected Gold Nanoclusters. *Acc. Chem. Res.* **2019**, *52*, 23−33.
(61) Agrachev, M.; Ruzzi, M.; Venzo, A.; Maran, F. Nuclear and Electron Magnetic Resonance Spectroscopies of Atomically Precise Gold Nanoclusters. *Acc. Chem. Res.* **2019**, *52*, 44−52.
(62) Hirai, H.; Takano, S.; Nakamura, T.; Tsukuda, T. Understanding Doping Effects on Electronic Structures of Gold Superatoms: A Case Study of Diphosphine-Protected M@Au12 (M = Au, Pt, Ir). *Inorg. Chem.* **2020**, DOI: 10.1021/acs.inorgchem.0c00879.
(63) Zeng, C.; Weitz, A.; Withers, G.; Higaki, T.; Zhao, S.; Chen, Y.; Gil, R. R.; Hendrich, M.; Jin, R. Controlling Magnetism of $Au_{133}(TBBT)_{52}$ Nanoclusters at Single Electron Level and Implication for Nonmetal to Metal Transition. *Chem. Sci.* **2019**, *10*, 9684−9691.
(64) Zhu, M.; Eckenhoff, W. T.; Pintauer, T.; Jin, R. Conversion of Anionic $[Au_{25}(SCH_2CH_2Ph)_{18}]^-$ Cluster to Charge Neutral Cluster via Air Oxidation. *J. Phys. Chem. C* **2008**, *112*, 14221−14224.
(65) Tlahuice-Flores, A. New Polyhedra Approach to Explain the Structure and Evolution on Size of Thiolated Gold Clusters. *J. Phys. Chem. C* **2019**, *123*, 10831−10841.
(66) Du, X.; Chai, J.; Yang, S.; Li, Y.; Higaki, H.; Li, S.; Jin, R. Fusion Growth Patterns in Atomically Precise Metal Nanoclusters. *Nanoscale* **2019**, *11*, 19158−19165.
(67) Liu, C.; Pei, Y.; Sun, H.; Ma, J. The Nucleation and Growth Mechanism of Thiolate-Protected Au Nanoclusters. *J. Am. Chem. Soc.* **2015**, *137*, 15809−15816.
(68) Zhou, M.; Higaki, T.; Hu, G.; Sfeir, M. Y.; Chen, Y.; Jiang, D.; Jin, R. Three-Orders-of-Magnitude Variation of Carrier Lifetimes with Crystal Phase of Gold Nanoclusters. *Science* **2019**, *364*, 279−282.

https://dx.doi.org/10.1021/jacs.0c09110
J. Am. Chem. Soc. XXXX, XXX, XXX−XXX